chemosensors

MDPI

Article

Quantitative Detection of ALP Activity via Electrochemiluminescence Signal Switching on a Biomimetic Zirconia Interface

Xinyu Lu [1], Jin Wang [1], Jiahao Zhou [2], Wenwen Tu [1], Junru Zhou [1] and Tianxiang Wei [2,3,*]

[1] School of Chemistry and Materials Science, Nanjing Normal University, Nanjing 210023, China
[2] School of Environment, Nanjing Normal University, Nanjing 210023, China
[3] State Key Laboratory of Analytical Chemistry for Life Science, Nanjing University, Nanjing 210023, China
* Correspondence: weitianxiang@njnu.edu.cn

Abstract

Quantitative detection of alkaline phosphatase (ALP) activity is crucial in clinical diagnosis and bioanalysis. Herein, we have developed a highly sensitive electrochemiluminescence (ECL) biosensor that employs a biomimetic zirconia interface as its core sensing platform. The interface was constructed by immobilizing o-phosphorylethanolamine (PEA) onto zirconium oxide nanofilms (ZrO_2NFs), forming a surface rich in Zr-O-P bonds. This design mimics phosphate recognition and enzyme-triggered dephosphorylation processes, where ALP catalyzes the hydrolysis of these bonds, triggering a direct switch in the ECL signal from $Ru(bpy)_3^{2+}$-loaded gold nanocage (Ru-AuNCs) emitters. This sensor achieves a wide linear range of 0.100–100 U/L and a low detection limit down to 0.0899 U/L. Its practical utility was validated through the accurate detection of ALP in fetal bovine serum samples, confirming high recovery and reliability. This strategy highlights the potential of biomimetic zirconia interfaces in developing robust biosensors for early disease diagnosis.

Keywords: ECL biosensing; alkaline phosphatase; Zr-O-P bond; bond cleavage

1. Introduction

Alkaline phosphatase (ALP) is a kind of hydrolase found in human bones, liver, and other organs, where it catalyzes the hydrolysis of various phosphorylated substances in the body, such as nucleic acids, proteins and so on. A typical dephosphorylation reaction catalyzed by ALP involves the reactant, the products, and a phosphate ion (Pi). There is a lot of evidence that the abnormal expression of ALP is closely associated with numerous diseases, including bone disease, liver disease, and even prostate cancer [1,2]. For example, the concentration for a normal person is below 190 mU/mL, while the level for some patients reaches 250 mU/mL [3]. Therefore, accurate determination of ALP is imperative in biomedical applications and the development of sensitive and reliable methods for ALP is a significant task. To date, researchers have proposed some methods for the detection of ALP, including chemiluminescence [4], surface-enhanced Raman scattering (SERS) [5], colorimetric assay [6], electrochemical methods [7], fluorescent detection [8,9], electrochemiluminescence (ECL) [10] and so on. Among these, ECL, which integrates the unique advantages of both electrochemical analysis and chemiluminescence analysis, has emerged as a powerful analytical technique due to its high sensitivity, fast response time, low cost, and low background interference [11–14]. It is widely applied in disease diagnosis, food safety, and environmental monitoring [15,16]. In recent years, the fabrication of

Check for updates

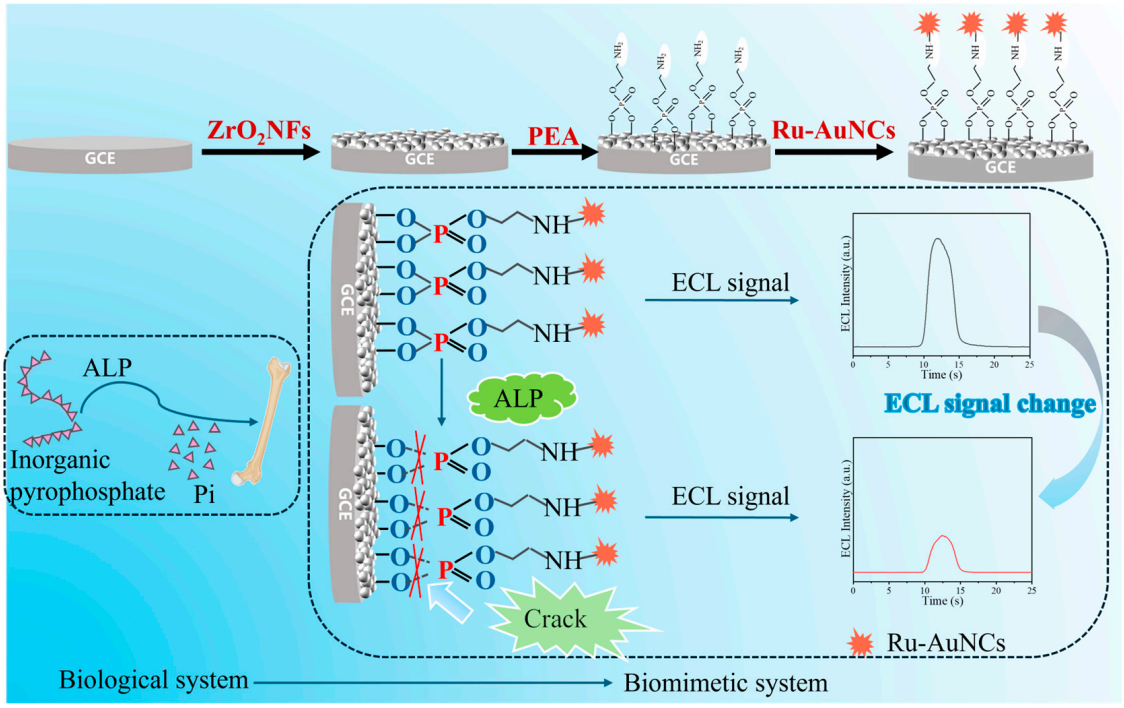
Received: 18 February 2026
Revised: 9 April 2026
Accepted: 10 April 2026
Published: 19 April 2026

Copyright: © 2026 by the authors. Licensee MDPI, Basel, Switzerland. This article is an open access article distributed under the terms and conditions of the Creative Commons Attribution (CC BY) license.

some sensors for ALP has required the participation of an additional enzyme for signal amplification [7,17]. However, the detection is limited by the time-consuming and tedious process and is susceptible to some environmental factors like temperature and pH, and thus does not meet the demands of point-of-care testing. In addition, the electron transfer at the electrode interface is also limited. Therefore, the rational construction of electrode interfaces for efficient electron transfer and signal amplification is desirable.

Metal oxides as electrode modification materials are popular owing to their ability to improve the specific surface area of the electrodes and enhance the electron transfer rate [18]. Among these, zirconium oxide (ZrO_2) has played a prominent role due to its excellent biocompatibility and chemical stability [19–22]. Notably, the unique phosphorus affinity of ZrO_2 is a key design concept that is critical to its selection as the substrate for the biomimetic interface. Our previous research has demonstrated that zirconium (Zr) exhibits a strong affinity for phosphate-containing groups, enabling efficient and specific recognition and immobilization through the formation of stable Zr-O-P bonds [23,24]. Interestingly, a previous study found that ALP can hydrolyze inorganic pyrophosphate (PPi), increasing the concentration of inorganic phosphate (pi), which is beneficial for mineralization [25,26]. Mimicking this key event, our biomimetic ZrO_2 interface is designed to undergo ALP-triggered hydrolysis of a surface-anchored phosphate ester, leading to a change in the interfacial properties that can be detected electrochemically. In this work, the core concept involves using o-phosphorylethanolamine (PEA) as a key hydrolysable molecular bridging unit. On one hand, its phosphate terminus forms a robust Zr-O-P linkage with zirconium oxide nanofilms (ZrO_2NFs), thereby stably constructing the biomimetic interface. On the other hand, its phosphoester bond serves as a specific enzymatic cleavage site for ALP. In the presence of ALP, it catalyzes the hydrolysis of the phosphoester bond in PEA [27], severing the molecular bridge and precisely triggering the switching of the physicochemical properties of the interface. So, in this work, the PEA acts as an analogue of PPi, which contains a hydrolysable P-O-P or P-O-C linkage recognized by ALP. Upon ALP catalysis, the PEA bridge is cleaved, altering the surface Ru-AuNCs density, generating an analogue to the pi in the natural system. This change in the chemical state of the interface then modulates the ECL signal, achieving direct ALP-responsive signal transduction that mimics the biological phosphate-based regulatory mechanism. This integrated design mimics the processes of specific recognition, the hydrolysis of phosphate-containing substrates by ALP, and the associated molecular recognition and signal transduction in biological systems, providing an innovative interfacial platform for constructing high-performance and highly selective ECL biosensors.

In a typical ECL system, luminophores, co-reactants, and the electrode interface are important components. $Ru(bpy)_3^{2+}$ is a common commercial ECL luminophore owing to its strong emission signal and recovery ability under cyclic potential scanning [28–30]. Nevertheless, the good solubility of $Ru(bpy)_3^{2}$ makes it difficult to fix the molecule on the electrode surface. In our previous work, we found that gold nanocages (AuNCs) can load more $Ru(bpy)_3^{2+}$ and produce steady and strong ECL signals [11]. In this work, we first synthesized the stable and excellent luminophores Ru-AuNCs. Then, ZrO_2NFs were electrodeposited on the glassy carbon electrode (GCE), providing abundant P binding sites, followed by efficient linking with PEA. Then Ru-AuNCs were fixed onto the electrode modified by ZrO_2NFs and PEA. When ALP is present, the phosphate ester bonds will be hydrolyzed, leading to the cleavage of Zr-O-P linkages and the detachment of Ru-AuNCs from the electrode surface. As a result, the increased distance between the luminophore and the electrode suppresses the electron transfer, decreasing the ECL intensity (Scheme 1). The fabricated sensor shows a wide linear range of 0.100–100 U/L and a low detection limit down to 89.9 mU/L, highlighting its proposing potential for early disease diagnosis.



Scheme 1. Strategy of the ECL biosensor for detecting ALP.

2. Materials and Methods

2.1. Materials and Reagents

Tris (2,2′-bipyridyl) ruthenium dichloride (II) hexahydrate (Ru (bpy)$_3$Cl$_2$·6H$_2$O), zirconium (IV) chloride oxide octahydrate (ZrOCl$_2$·8H$_2$O), thiol polyethylene glycol thiol (HS-PEG-SH, Mw ≈ 5000 Da), dopamine hydrochloride (DA), glutathione (reduced, GSH), acetic acid (HAC), sodium acetate (NaAC), hydrochloric acid (HCl) and o-phosphorylethanolamine (PEA) were purchased from Aladdin (Shanghai, China). Tripropylamine (TPrA), gold trihydrate (III) (HAuCl$_4$·3H$_2$O), polyvinylpyrrolidone (PVP, Mw ≈ 29,000, 55,000), acetylcholinesterase (AchE), glutathione S-transferase (GST), glucose oxidase (GOx), bovine serum albumin (BSA), β-galactosidase (GAL), tris(hydroxymethyl) aminomethane hydrochloride (Tris) and Nafion (D-520 dispersion, 5% w/w in water and 1-propanol, ≥1.00 meq/g exchange capacity) were obtained from Sigma-Aldrich (St. Louis, MO, USA). ALP was obtained from Machlin. Na$_2$S·9H$_2$O, NaH$_2$PO$_4$, Na$_2$HPO$_4$, K$_3$Fe(CN)$_6$, K$_4$Fe(CN)$_6$, KCl, NaCl, AgNO$_3$, ethylene glycol and ascorbic acid (AA) were purchased from Sinopharm (Shanghai, China). Fetal bovine serum (FBS) was purchased from Gibco (Waltham, MA, USA). All purchased chemicals and solvents were at least analytical-grade and were used directly in the experiments without any treatment. All ultrapure water was treated with a Millipore-Q purification system.

2.2. Characterization

The ECL and cyclic voltammetry (CV) data were collected on MPI-A instrumentation (Xi'an Remax Electronic Science & Technology Co., Ltd., Xi'an, China) with a classic three-electrode system, which includes a GCE (4 mm in diameter) as the working electrode, an Ag/AgCl (saturated KCl aqueous) as the reference electrode, and a platinum rod as the counter electrode. The scanning electron microscope (SEM) images were acquired by a Nova NanoSEM 450 (FEI, Hillsboro, OR, USA). The transmission electron microscope (TEM) images were obtained on a H7650 apparatus (Hitachi, Tokyo, Japan) at an accelerating voltage of 80 kV. The X-ray photoelectron spectroscopy (XPS) spectrum was obtained by the ESCALAB Xi system (Thermo Fisher Scientific, Waltham, MA, USA). Electrochemical

impedance spectroscopy (EIS) was carried out by an Autolab potentiostat/galvanostat PGSTAT302N workstation (Metrohm, Utrecht, The Netherlands) from 0.1 Hz to 100 kHz in KCl solution (0.1 M) containing a $K_3Fe(CN)_6/K_4Fe(CN)_6$ (5.0 mM, 1:1) as a redox probe with an amplitude of 0.005 V. Zeta potential analysis was performed using a Nano-Zetasizer (Malvern instruments, Malvern, UK).

2.3. Synthesis of AuNCs

Firstly, the silver nanocubes (AgNCs) were obtained based on a previously published report [11]. Ethylene glycol (6 mL) was heated to 150 °C. Then, the Na_2S solution (100 μL, 3 mM) was added and reacted for 10 min. Afterwards, the PVP solution (1.5 mL, 20 mg/mL (Mw ≈ 29,000)) and the $AgNO_3$ solution (0.5 mL, 48 mg/mL) were pipetted into the mixture. The reaction was conducted in a water bath at room temperature for 10 to 15 min. Then, the mixture was centrifuged for 30 min at 2000 *g*. Later, the settled material was washed with water three times and centrifuged at 9000 *g* for 8 min. Then, the washed AgNCs were transferred to a scintillation vial and diluted to 4 mL with ultrapure water. AuNCs were obtained by a galvanic replacement reaction using AgNCs as sacrificial templates as follows: The as-stored AgNCs dispersion (200 μL) was added into the PVP solution (10 mL, 1 mg/mL, Mw ≈ 55,000), which was heated, and $HAuCl_4$ solution (0.1 mM, 1.2 mL) was slowly added for 5 min. After the experiment finished, the solution was cooled to room temperature, followed by centrifugation at 14,000 rpm for 15 min; it was then washed 3 times with water.

2.4. Functionalization of AuNCs for $Ru(bpy)_3^{2+}$ Loading

$Ru(bpy)_3Cl_2$ (500 μL, 10 mM) was added to the AuNCs pellet and the mixture was sonicated for 30 min. Next, HS-PEG-SH (500 μL, 30 mg/mL) was added, and the reaction lasted for 45 min at 4 °C, and then mixture was centrifuged at 12,000 rpm and washed with water.

2.5. Preparation of the ZrO_2NFs-Modified GCE Electrode

The ZrO_2NFs were synthesized based on previously published research [31]. The GCE was polished with aluminum oxide powder (0.3 and 0.05 μm) and was ultrasonicated in ethanol and water for 1 min, respectively. A ZrO_2NFs film was electrochemically deposited on the GCE by CV with potential scanning between −1.1 and 1.15 V (vs. saturated calomel electrode, SCE) with a sweep rate of 50 mV s^{-1} at room temperature for 10 cycles in a fresh aqueous solution containing 5.0 mM $ZrOCl_2$ and 0.1 M KCl. An inert atmosphere was maintained by passing N_2 over the solution during the experiments. In the whole experiment, the error bar represents the standard deviation (SD) of measurements.

2.6. Construction of the ECL Biosensor

PEA (20 μL, 30 mg/mL) was dropped on the ZrO_2NFs/GCE and incubated at 37 °C for 2 h. Then, Ru-AuNCs (10 μL, 1.0 mg/mL) were added and incubated at 37 °C for 1 h. The obtained Ru-AuNCs/PEA/ZrO_2NFs/GCE were incubated with ALP with different concentrations for 10 min, followed by gentle washing with buffer (PBS, pH 7.4) solution before testing. For ECL measurement, the ECL biosensor for ALP was carried out in a quartz cell with 0.1 M buffer solution (pH 8.5) containing 10 mM TPrA as a co-reactant at room temperature. A voltage of 800 V was recommended for the photomultiplier tube (PMT), and the continuous potential range was intended to be from 0 to 1.0 V (vs. Ag/AgCl (saturated KCl aqueous)) at a scan rate of 100 mV/s.

3. Results and Discussion

3.1. Characterization of ZrO_2NFs and ZrO_2NF-Modified GCE

SEM was employed to investigate the nature of the ZrO_2NFs nanocomposite film. Figure 1A shows the smooth and flat GCE surface (Figure 1A). The typical SEM images of ZrO_2NFs film (Figure 1B,C) compared with bare ITO (Figure 1A) showed that ZrO_2NFs grew regularly and uniformly and presented nodule-like nanoparticle morphology. In addition, the CV responses for the formation processes of the formed ZrO_2NFs on the GCE (Figure S1) showed a cathodic peak and the emergence of an irreversible peak at around 0.55 V (vs. SCE), which corresponded to the reduction of water at the electrode surface, generating OH^- and inducing a pH increase. The alkalinity promoted the hydrolysis of $ZrOCl_2$, leading to the precipitation of ZrO_2 on the electrode surface, in which the element Zr remained at a +4 state during the deposition process [31–33], in which the hydrolysis of $ZrOCl_2$ could take place as the following equation (1) [32]:

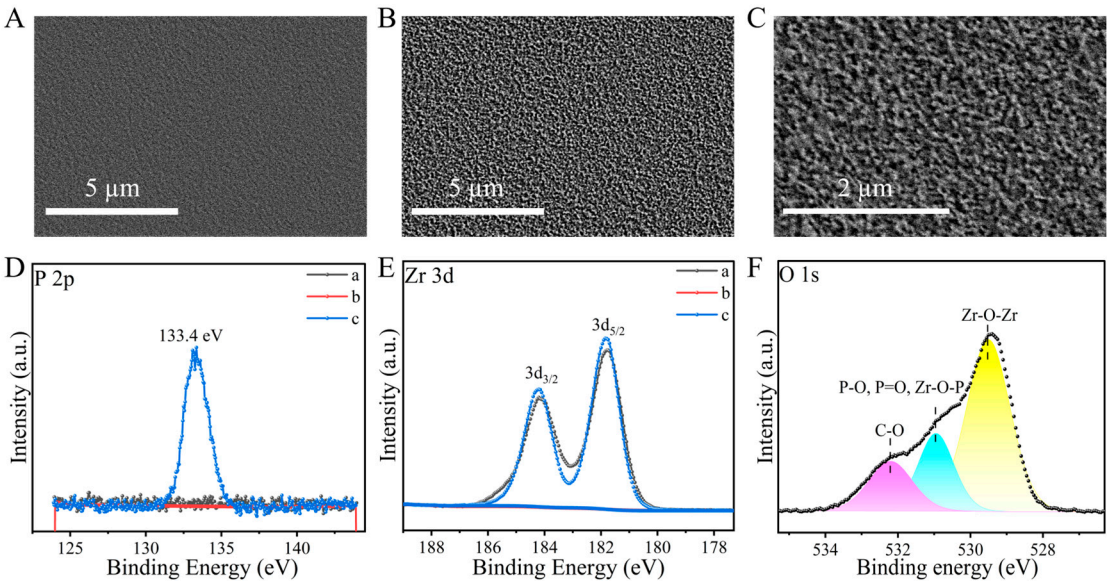


Figure 1. (**A**) SEM of ITO. (**B**,**C**) SEM images of the electrodeposited ZrO_2NFs onto ITO. (**D**–**F**) High-resolution P 2p, Zr 3d, and O 1s XPS spectra of ZrO_2NFs and ZrO_2NFs with PEA (curve a: ZrO_2NFs, curve b: background, and curve c: ZrO_2NFs with PEA).

$$ZrOCl_2 + H_2O = ZrO_2 + 2HCl \quad (1)$$

The connection between the ZrO_2NFs and PEA molecules was further characterized by XPS. Figure 2D–F present the high-resolution P 2p, Zr 3d, and O 1s XPS spectra of ZrO_2NFs and ZrO_2NFs connected with PEA. What can be observed is the obvious P 2p peak for ZrO_2NFs/PEA compared with ZrO_2NFs (Figure 1D), implying the successful connection of PEA onto ZrO_2NFs. For the Zr 3d spectra for ZrO_2NFs and ZrO_2NFs/PEA, the red shift of the Zr 3d peak indirectly indicated the successful combination of ZrO_2NFs and PEA (Figure 1E). The reason for the phenomenon of red shift is mainly due to the difference in electronegativity. Briefly, the electronegativity of Zr is inferior to that of P, and the existence of Zr-O-P bonds reduces the electron cloud density at Zr, which impairs the shielding effect from external electrons and enhances the binding energy. This phenomenon and the reason behind it were consistent with our previous report [23]. In addition, the peak at 531 eV for O 1s further verifies the formation of Zr-O-P bonds (Figure 1F) [23,34]. The above characterization demonstrated the successful combination of PEA and ZrO_2NFs in the role of Zr-O-P bonds.

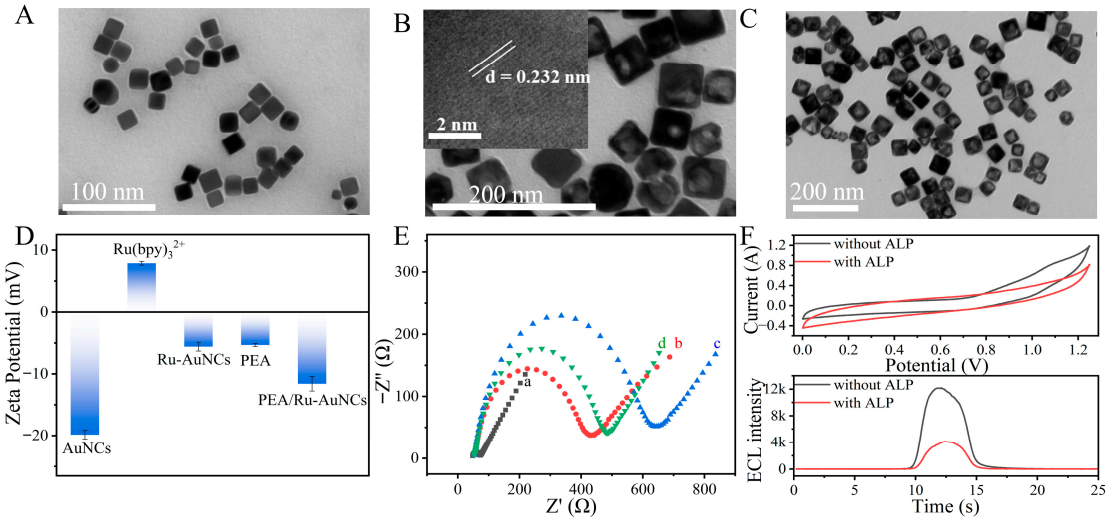


Figure 2. TEM images of (**A**) AgNCs, (**B**) AuNCs, and (**C**) Ru-AuNCs. (**D**) The comparison of zeta potential of AuNCs, $Ru(bpy)_3^{2+}$, Ru-AuNCs, PEA and PEA/RuAuNCs (n = 3). (**E**) EIS curves of the bare GCE (curve a), ZrO_2NFs/GCE (curve b), Ru-AuNCs/PEA/ZrO_2NFs/GCE (curve c), and Ru-AuNCs/PEA/ZrO_2NFs/GCE with ALP (curve d). (**F**) The CV curves and ECL responses with and without ALP.

3.2. Characterization of the Constructed ECL Sensor

TEM was used to characterize the morphology of AgNCs, AuNCs, and Ru-AuNCs (Figure 2). Figure 2A shows that AgNCs possess a cubic structure with a uniform diameter of about 45 nm. For AuNCs, Figure 2B displays the unique topology of the hollow structure with a diameter of about 45 nm. The lattice stripe spacing of AuNCs was 0.232 nm (Figure 2B insert), which was affiliated with the (111) lattice plane of Au [35]. The above characterization demonstrates the successful conversion from AgNCs to AuNCs by the galvanic replacement reaction. The introduction of the Ru element did not change the structure of AuNCs (Figure 2C), which is consistent with our previous report [11].

To demonstrate the successful connection of each component, Zeta potential measurements were used to characterize the successful fabrication of the ECL electrode interface (Figure 2D). It showed that the potentials were −19.9 mV, 7.86 mV, and −5.60 mV for AuNCs, $Ru(bpy)_3^{2+}$, and Ru-AuNCs, respectively, which manifested that the Ru-AuNCs were easy to form under the electrostatic interaction due to the opposite potential of AuNCs and $Ru(bpy)_3^{2+}$. Subsequently, a strong Au-S bond can form between the thiol group (-SH) and AuNCs. In addition, SH-PEG-SH can promote the formation of a loop structure, preventing the aggregation of AuNCs [36] (Scheme S1). For the interaction between NH_2 and Ru-AuNCs, it relied on hydrogen bond formation between NH_2 and SH-PEG-SH on Ru-AuNCs [37]. Furthermore, when PEA was linked to Ru-AuNCs, the negative potential of PEA conferred more negative potential (−11.6 mV) to Ru-AuNCs, which further demonstrated that PEA was modified on Ru-AuNCs successfully. In addition, EIS is an essential tool to characterize the interfacial properties of modified electrodes. In the EIS curves, the semicircle part at high frequency represented the charge transfer resistance and the line part at low frequency represented the diffusion process [38]. As shown in Figure 2E, the bare GCE (curve a) showed a low electron transfer resistance (R_{et} value of 45.0 Ω). When the ZrO_2NFs film was successfully electrodeposited on the GCE surface, the fitted R_{et} value rose to 352 Ω (curve b), which demonstrated that ZrO_2NFs caused blockage in the electron transfer at the electrode surface. Subsequently, with the modification of PEA and Ru-AuNCs, the impedance of the electrodes increased to 554 Ω (curve c). Then, after ALP treatment and washing, the Zr-O-P bonds were broken under the hydrolysis of ALP,

which caused most of the Ru-AuNCs material to move away from the electrode surface and led to the impedance of the electrodes decreasing to 400 Ω (curve d). These modifications indicate that an ECL biosensor has been successfully constructed to detect ALP.

To better investigate the ECL sensor of ALP, ECL and CV performance assessments were carried out. As shown in Figure 2F, it can be observed that an oxidation peak at about 1.07 V corresponded to the oxidation of TPrA, confirming that ECL emission originated from Ru-AuNCs and the co-reactant pathway. Understanding the mechanism is imperative to design efficient sensors. As in our previous work, we found that the ECL mechanism mainly results from the redox reaction between luminophores and TPrA. In this work, the luminophores Ru-AuNCs and TPrA are oxidized by losing electrons on the electrode surface firstly, producing Ru-AuNCs^{+} and TPrA*$^{+}$, respectively. Then, deprotonation of TPrA*$^{+}$ generated the reduced state (TPrA*), which was used to reduce Ru-AuNCs^{+} to achieve the excited state Ru-AuNCs*. Ultimately, the unstable Ru-AuNCs* emitted an ECL signal from the excited state to the ground state [11]. After ALP treatment, the current decreased. At the same time, the ECL signal decreased at the introduction of ALP, which is due to the cleavage of Zr-O-P bonds; this increased the distance between the luminophore and the electrode and weakened the ECL signal.

3.3. Performance of the ECL Biosensor

3.3.1. Optimization of Experimental Conditions

To improve the sensitivity of the ECL sensors, we optimized the content of Ru-AuNCs, PEA, and TPrA, and we also optimized the CV cycles of ZrO_2NFs, the incubation time and the pH, as shown in Figure 3. The optimization of Ru-AuNCs concentration was carried out in 10 mM TPrA using electrodes modified with ZrO_2NFs (deposition cycles were chosen as 10) and PEA (30 mg/mL) with ALP incubation time at 10 min, following the variation of the concentration of Ru-AuNCs from 0.2 to 1.2 mg/mL. It can be seen in Figure 3A that the concentration of Ru-AuNCs was related to the ECL signal and directly affected the detection performance of the ECL biosensor, which showed that the intensity of the ECL response increased with the Ru-AuNCs concentration until the concentration was up to 1.0 mg/mL. When the concentration of Ru-AuNCs was higher than 1 mg/mL, the ECL signal did not change, which may be due to stacked layers being too thick to block the interfacial electron transfer [39]. Therefore, the concentration of Ru-AuNCs (1.0 mg/mL) was chosen. Since the state and quantity of ZrO_2NFs film formation on the electrode surface were influenced by the electrodeposition time [40], we optimized the CV scan cycle number during the formation of ZrO_2NFs film by electrodeposition (Figure 3B). For the optimization of CV scan cycles, the number of scan cycles varied from 2 to 12 with 1 mg/mL for the concentration of Ru-AuNCs, 30 mg/mL for PEA concentration, 10 min for incubation time, and pH 8.5 for the buffer solution containing 10 mM TPrA. The ECL intensity gradually increased with the increase in cycles until the number of cycles reached 10. When there were more than 10 cycles, the ECL intensity decreased, which may be because of the limited electron transfer due to the thickness of the films. So, the number of CV scan cycles performed for the electrodeposition of ZrO_2NFs was 10. The PEA is an important molecule that played a connecting role in the assembly process of the sensor. Its presence had a direct effect on the stability of the material connection, and then affected the ECL signal of sensor, so we also optimized the concentration of PEA. For the optimization of the concentration of PEA, the experiment was carried out at varied concentrations of PEA from 10 to 35 mg/mL at scan cycles 10, with a 1 mg/mL Ru-AuNCs concentration, incubation time of 10 min, and pH 8.5 for the buffer solution containing 10 mM TPrA. The relationship between the ECL intensity and PEA concentration (Figure 3C) indicated that when the PEA concentration increased to 30 mg/mL, the ECL intensity gradually increased and eventually became

constant. So, the concentration of PEA was selected as 30 mg/mL. After the successful sensor assembly, we needed to co-incubate ALP at different concentrations in the detection process to enable the sensor to play its role. Insufficient incubation prevents the sensor from performing fully. The incubation time refers to the process of placing ALP with the sensing interface Ru-AuNCs/PEA/ZrO_2NFs/GCE materials in PBS buffer solution (pH = 7.4) for a certain period of time. Therefore, we further investigated the co-incubation time of the sensor with ALP (Figure 3D). For the optimization of the incubation time, the experiment was performed at varied incubation times from 2 to 12 min, following a concentration of 1mg/mL for Ru-AuNCs, 10 cycles for the CV scan cycles, 30 mg/mL for PEA concentration, and pH 8.5 for the buffer solution containing 10 mM TPrA. The ECL intensity increased with the extension of ALP incubation time and remained constant after 10 min. Thus, the optimum incubation time was 10 min.

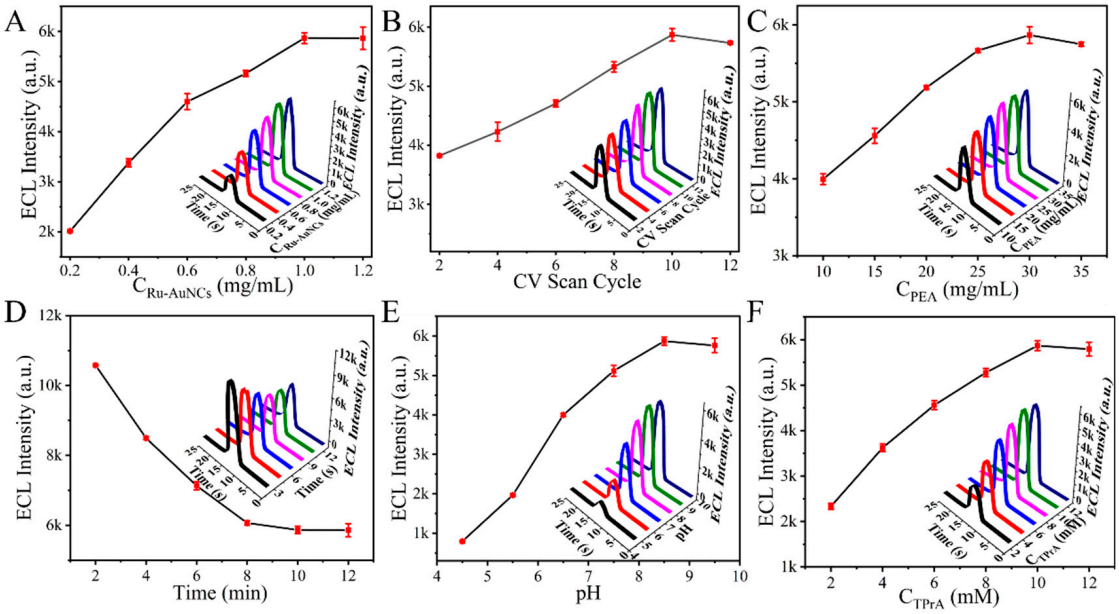


Figure 3. Optimization of parameters in the ECL biosensor of (**A**) concentration of Ru-AuNCs, (**B**) CV scan cycle of ZrO_2NFs film, (**C**) concentration of PEA, (**D**) incubation time for ECL measurement, (**E**) different pH values, and (**F**) concentration of TPrA (n = 3).

In addition, some measurement conditions of the ALP ECL biosensor were also investigated. For the optimization of pH, we carried out experiments at different pH values from 4.5 to 9.5 (the buffer solution at different pH values was adjusted by HAC-NaAC buffer in the range of 4.5–5.5, PBS buffer in 6.5–8.0, and Tris-HCl buffer when the pH was over 8, respectively) with a 1 mg/mL Ru-AuNCs concentration, 10 cycles for scan cycles, a 30 mg/mL PEA concentration, a 10 min incubation time, and a 10 mM TPrA concentration. For the optimization of TPrA concentration, it was performed under the same conditions as above, except that the TPrA concentration was varied from 2 to 12 mM at pH 8.5. The effect of pH and TPrA concentration on the ALP ECL biosensor (Figure 3E,F) showed that the ECL intensity was the strongest when the pH value was 8.5 and the TPrA concentration was 10 mM. Consequently, a 0.1 M phosphate solution with a pH of 8.5 and 10 mM TPrA concentration was used throughout the assay.

3.3.2. Detection of ALP with the ECL Biosensor

Under the optimal conditions, the ECL biosensor was used for ALP detection with different concentrations by measuring ECL responses. The ECL signals (Figure 4A) showed that the ECL intensity gradually decreased with the increasing concentration of ALP in the

range of 0.100 U/L to 100 U/L in 0.1 M buffer solution (pH 8.5) containing 10 mM TPrA. The ECL signals (Figure 4B) showed a good linear relationship with the logarithm of ALP concentration, while the calibration equation was $\Delta E = 3.52 \times 10^3 - 2.77 \times 10^3$ lg[ALP] ($R^2 = 0.998$) with a detection limit of 0.0899 U/L (S/N = 3). Here, $\Delta E = E_0 - E_1$, where E_0 was the initial ECL signal without ALP and E_1 was the ECL signal response to ALP.

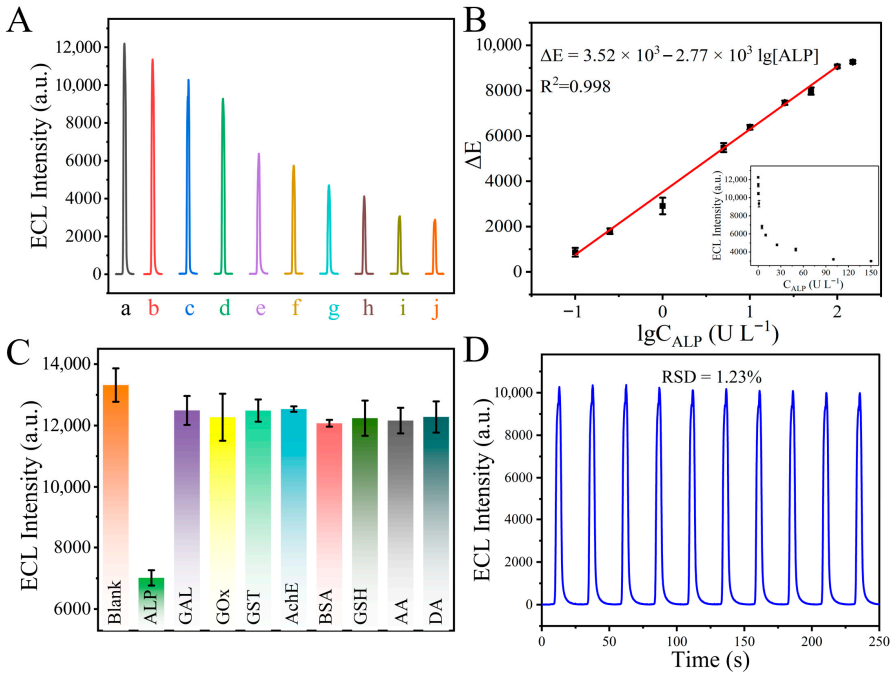


Figure 4. (**A**) ECL values versus different concentrations of ALP ((a) 0, (b) 0.10, (c) 0.25, (d) 1.0, (e) 5.0, (f) 10, (g) 25, (h) 50, (i) 100, and (j) 150 U/L). (**B**) Linear calibration plot of ΔE (n = 3). (**C**) Bar graph for the specificity of the ECL biosensor for ALP detection: control, ALP (10.0 U/L), GAL (100 U/L), GOx (100 U/L), GST (100 U/L), AchE (100 U/L), BSA (1 mg/mL), GSH (20 mM), AA (20 mM), and DA (20 mM) (n = 3). (**D**) Stability of the ECL biosensor under 10 consecutive cyclic potential scans.

To evaluate its specificity, the ECL biosensor was challenged with various potential interferents, including four other enzymes (GAL, GST, GOx, and AChE), BSA, and three small molecules (GSH, AA, and DA). The ECL responses of this ECL biosensor (Figure 4C) were obtained in 10 U/L ALP, 100 U/L GAL, 100 U/L GOx, 100 U/L GST, 100 U/L AchE, 1 mg/mL BSA, 10 mM GSH, 10 mM AA, and 10 mM DA. The stability of the ALP biosensor (Figure 4D, with 1.0 U/L ALP) was further tested by performing 10 cycles of continuous ECL scans. There was no significant change in the ECL peak, and the RSD was 1.23%. All of these results demonstrated the sensor's excellent performance with superior selectivity and stability. In addition, we have compared the sensor's performance with other detection methods, as shown in Table 1. From Table 1, it can be seen that the constructed ECL sensor for ALP detection displayed a wider linear detection range and lower detection limit, which is in favor of the disease diagnosis in the future.

Table 1. Comparison of the analytical performance of different techniques in ALP detection.

Method	Linear Range (U/L)	LOD (U/L)	Reference
EC	20–100	1.48	[7]
SERS	0.1–70	0.079	[41]
Colorimetry	0.5–8	0.46	[42]
FL	0.1–50	0.075	[43]

Table 1. *Cont.*

Method	Linear Range (U/L)	LOD (U/L)	Reference
FL	1–100	0.1	[44]
CL	0.08–5	0.049	[45]
ECL	0.1–6	0.037	[46]
ECL-RET	5–50	0.8	[47]
FL	20–180	2.3	[48]
Chemiluminescence imaging	-	0.039	[49]
ECL	0.100–100	0.090	This work

The detection of ALP in actual samples was an important index with which to evaluate the analytical performance of the biosensor. As shown in Table S1, 1.00, 3.00, 5.00, 10.0, and 20.0 U/L ALP were spiked into FBS, and the results were in good agreement with the total amount. The recovery rate of the standard addition was 99.5 -113%, which showed that the method was applicable for the detection of ALP in actual samples.

4. Conclusions

In summary, a simple and effective ECL sensor for ALP was constructed based on ZrO_2NFs-PEA-Ru-AuNCs biomimetic interface. The fabrication of the ECL sensor was based on the strategy of the cleavage of Zr-O-P bonds under the hydrolysis of ALP, which weakens the ECL intensity, showing a wide linear range (0.100–100 U/L) with a low limit of detection (89.9 mU/L). The sensor displayed superior selectivity and stability and can be used for the detection of ALP in fetal bovine serum samples with satisfactory results, demonstrating the potential for disease diagnosis.

Supplementary Materials: The following supporting information can be downloaded at: https://www.mdpi.com/article/10.3390/chemosensors14040098/s1, Figure S1: Cyclic voltammograms of 5 mM ZrOCl2 at GCE in 0.1 M KCl aqueous solutions at a scan rate of 50 mV/s (the dotted line represented the position of the cathodic peak); Scheme S1: (A) Scheme illustration of chemical structure of SH-PEG-SH and Au. (B) Scheme illustration of the role of SH-PEG-SH on the aggregation of AuNCs; Table S1: Detection of ALP in FBS (n = 3).

Author Contributions: Conceptualization, T.W.; methodology, W.T., J.W., X.L., and T.W.; validation, J.W., X.L., J.Z. (Jiahao Zhou), W.T., and T.W.; formal analysis, X.L., W.T., J.W., and J.Z. (Junru Zhou); investigation, J.W., X.L., J.Z. (Junru Zhou), J.Z. (Jiahao Zhou), and T.W.; resources, T.W.; data curation, X.L., J.Z. (Jiahao Zhou), J.Z. (Junru Zhou), and W.T.; writing-original draft preparation, X.L., J.W., and J.Z. (Junru Zhou); writing-review and editing, T.W. and W.T. All authors have read and agreed to the published version of the manuscript.

Funding: This work was financially supported by the National Natural Science Foundation of China (22234005), the Qing Lan Project of Jiangsu Province, the Postgraduate Research and Practice Innovation Program of Jiangsu Province (KYCX25-1949), and the Undergraduate Innovation Training Program of Nanjing Normal University (202610319205).

Institutional Review Board Statement: Not applicable.

Informed Consent Statement: Not applicable.

Data Availability Statement: The original contributions presented in this study are included in the article material. Further inquiries can be directed to the corresponding author.

Conflicts of Interest: The authors declare no conflicts of interest.

References

1. Chen, C.; Yuan, Q.; Ni, P.; Jiang, Y.; Zhao, Z.; Lu, Y. Fluorescence assay for alkaline phosphatase based on ATP hydrolysis-triggered dissociation of cerium coordination polymer nanoparticles. *Analyst* **2018**, *143*, 3821–3828. [CrossRef]
2. Deng, J.; Yu, P.; Wang, Y.; Mao, L. Real-time ratiometric fluorescent assay for alkaline phosphatase activity with stimulus responsive infinite coordination polymer nanoparticles. *Anal. Chem.* **2015**, *87*, 3080–3086. [CrossRef]
3. Zhang, Y.; Li, P.; Lu, J.; Li, D.; Yang, H.; Li, X.; Liu, Y. A novel electrochemical platform for assay of alkaline phosphatase based on amifostine and ATRP signal amplification. *Anal. Bioanal. Chem.* **2022**, *414*, 6955–6964. [CrossRef]
4. Zhang, Q.; Zhang, C.; Yang, M.; Yu, D.; Yu, C. Pyrophosphate as substrate for alkaline phosphatase activity: A convenient flow-injection chemiluminescence assay. *Luminescence* **2017**, *32*, 1150–1156. [CrossRef] [PubMed]
5. Xi, C.-Y.; Zhang, M.; Jiang, L.; Chen, H.-Y.; Lv, J.; He, Y.; Hafez, M.E.; Qian, R.-C.; Li, D.-W. MOFs-functionalized regenerable SERS sensor based on electrochemistry for pretreatment-free detection of serum alkaline phosphatase activity. *Sens. Actuators B Chem.* **2022**, *369*, 132264. [CrossRef]
6. Wang, X.; Jiang, X.; Wei, H. Phosphate-responsive 2D-metal–organic-framework-nanozymes for colorimetric detection of alkaline phosphatase. *J. Mater. Chem. B* **2020**, *8*, 6905–6911. [CrossRef]
7. Wang, W.; Lu, J.; Hao, L.; Yang, H.; Song, X.; Si, F. Electrochemical detection of alkaline phosphatase activity through enzyme-catalyzed reaction using aminoferrocene as an electroactive probe. *Anal. Bioanal. Chem.* **2021**, *413*, 1827–1836. [CrossRef]
8. Tan, Y.; Zhang, L.; Man, K.H.; Peltier, R.; Chen, G.; Zhang, H.; Zhou, L.; Wang, F.; Ho, D.; Yao, S.Q.; et al. Reaction-based off–on near-infrared fluorescent probe for imaging alkaline phosphatase activity in living cells and mice. *ACS Appl. Mater. Interfaces* **2017**, *9*, 6796–6803. [CrossRef] [PubMed]
9. Zhang, H.; Ju, Q.; Pang, S.; Wei, N.; Zhang, Y. Recent progress of fluorescent probes for the detection of alkaline phosphatase (ALP): A review. *Dye. Pigment.* **2021**, *194*, 109569. [CrossRef]
10. Yang, X.-Y.; Bai, Y.-Y.; Huangfu, Y.-Y.; Guo, W.-J.; Yang, Y.-J.; Pang, D.-W.; Zhang, Z.-L. Ultrasensitive electrochemiluminescence biosensor based on closed bipolar electrode for alkaline phosphatase detection in single liver cancer cell. *Anal. Chem.* **2020**, *93*, 1757–1763. [CrossRef] [PubMed]
11. Wang, J.; Lu, X.; Wang, H.; Zhong, Y.; Dai, Z.; Wei, T. Target-induced reconstruction of $Ru(bpy)_3^{2+}$-loaded gold nanocage for one-step highly sensitive detection of Hg^{2+}. *Talanta* **2025**, *292*, 127955. [CrossRef]
12. Sun, H.; Guan, J.; Chai, H.; Yu, K.; Qu, L.; Zhang, X.; Zhang, G. Zinc porphyrin/MXene hybrids with phosphate-induced stimuli-responsive behavior for dual-mode fluorescent/electrochemiluminescent ratiometric biosensing. *Biosens. Bioelectron.* **2024**, *251*, 116080. [CrossRef]
13. Zhang, L.; Gao, W.; Zhang, L.; Ma, X.; Zhang, Y.; Zhu, P.; Yu, J. Self-enhanced electrochemiluminescence microreactors based on bimetallic porphyrin covalent organic frameworks for microRNA detection. *J. Anal. Test.* **2025**, *9*, 635–645. [CrossRef]
14. Li, X.; Li, G.; Wu, S.; Cao, X.; Sun, D.; Li, S.; Chen, L.; Zhang, J.; Gao, H.; Wei, P.; et al. Sensitive and rapid electrochemiluminescent detection of choline based on luminol derivate-doped silica nanoparticles. *J. Anal. Test.* **2025**, *9*, 421–427. [CrossRef]
15. Wang, X.; Cao, Z.; Li, H.; Zhao, S.; Wang, C.; Wang, D.; Liu, W.; Ding, S. Recent advances in single-atom catalysts-based electrochemiluminescence sensors. *Coord. Chem. Rev.* **2026**, *546*, 217066. [CrossRef]
16. Zhang, X.; Ma, J.; Zhou, S.; Yang, H.; Yu, J.; Zhang, Y. Organic frameworks-based electrochemiluminescence sensors for point-of-care testing. *Coord. Chem. Rev.* **2026**, *546*, 217098. [CrossRef]
17. Shi, Y.; Yang, M.; Liu, L.; Pang, Y.; Long, Y.; Zheng, H. GTP as a peroxidase-mimic to mediate enzymatic cascade reaction for alkaline phosphatase detection and alkaline phosphatase-linked immunoassay. *Sens. Actuators B Chem.* **2018**, *275*, 43–49. [CrossRef]
18. Singh, K.; Maurya, K.K.; Malviya, M. Review of electrochemical sensors and biosensors based on first-row transition metals, their oxides, and noble metals nanoparticles. *J. Anal. Test.* **2023**, *8*, 143–159. [CrossRef]
19. Dong, X.; Zhang, X.; Du, Y.; Liu, J.; Zeng, Q.; Cao, W.; Wei, Q.; Ju, H. Zirconium dioxide as electrochemiluminescence emitter for D-dimer determination based on dual-quenching sensing strategy. *Biosens. Bioelectron.* **2023**, *236*, 115437. [CrossRef] [PubMed]
20. Zhang, L.; Wu, L.; Li, T.; Wang, S.; Ye, Z.; Wang, B.; Qin, P.; Du, M.; Feng, Q.; Cai, C.; et al. Fe-Zn co-doping creates highly active interfaces on ZrO_2 for efficient CO_2 hydrogenation to methanol. *Sci. China-Chem.* **2026**. [CrossRef]
21. Xiao, W.; Acharya, D.; Hou, J.; Li, H.; Wang, Z.; Huang, X.; Qu, K.; Sun, D. Epitaxial growth of high-nuclearity zirconium oxo clusters from Zr16 to Zr20 and subsequent ligand exchange. *Sci. China Chem.* **2025**, *69*, 166–173. [CrossRef]
22. Zhang, Z.; Ma, H.; Mo, H.; Zhu, N. Organophosphorus pesticide photoelectrochemical/electrochemical dual-mode smartsensors derived from synergistic Co,N-TiO_2@ZrO_2/3DGH platform. *Chemosensors* **2025**, *13*, 167. [CrossRef]
23. Yu, K.; Wei, T.; Li, Z.; Li, J.; Wang, Z.; Dai, Z. Construction of molecular sensing and logic systems based on site-occupying effect-modulated MOF–DNA interaction. *J. Am. Chem. Soc.* **2020**, *142*, 21267–21271. [CrossRef]
24. Wei, T.; Zhang, Y.; Wang, H.; Li, H.; Fang, T.; Wang, Z.; Dai, Z. Self-assembled electroactive MOF–magnetic dispersible aptasensor enables ultrasensitive microcystin-LR detection in eutrophic water. *Chem. Eng. J.* **2023**, *466*, 142809. [CrossRef]

25. Ansari, S.; Ito, K.; Hofmann, S. Alkaline phosphatase activity of serum affects osteogenic differentiation cultures. *ACS Omega* **2022**, *7*, 12724–12733. [CrossRef]
26. Alcantara, E.H.; Kwon, J.H.; Kang, M.K.; Cho, Y.E.; Kwun, I.S. Zinc deficiency promotes calcification in vascular smooth muscle cells independent of alkaline phosphatase action and partly impacted by Pit1 upregulation. *Nutrients* **2024**, *16*, 291. [CrossRef] [PubMed]
27. Si, F.; Zhang, Y.; Lu, J.; Hou, M.; Yang, H.; Liu, Y. A highly sensitive, eco-friendly electrochemical assay for alkaline phosphatase activity based on a photoATRP signal amplification strategy. *Talanta* **2023**, *252*, 123775. [CrossRef] [PubMed]
28. Kirschbaum, S.E.K.; Baeumner, A.J. A review of electrochemiluminescence (ECL) in and for microfluidic analytical devices. *Anal. Bioanal. Chem.* **2015**, *407*, 3911–3926. [CrossRef]
29. Liu, Y.; Guo, W.; Su, B. Recent advances in electrochemiluminescence imaging analysis based on nanomaterials and micro-/nanostructures. *Chin. Chem. Lett.* **2019**, *30*, 1593–1599. [CrossRef]
30. Miao, W.; Choi, J.-P.; Bard, A.J. Electrogenerated chemiluminescence 69: The tris(2,2′-bipyridine)ruthenium(II), $(Ru(bpy)_3^{2+})$/tri-n-propylamine (TPrA) system revisiteds-a new route involving $TPrA^{\bullet+}$ cation radicals. *J. Am. Chem. Soc.* **2002**, *124*, 14478–14485. [CrossRef]
31. Nie, T.; Zhang, K.; Xu, J.; Lu, L.; Bai, L. A facile one-pot strategy for the electrochemical synthesis of poly(3,4-ethylenedioxythiophene)/Zirconia nanocomposite as an effective sensing platform for vitamins B2, B6 and C. *J. Electroanal. Chem.* **2014**, *717–718*, 1–9. [CrossRef]
32. Yu, H.-Z.W.; Rowe, A.M.; Waugh, D. Templated electrochemical deposition of zirconia thin films on "recordable CDs". *Anal. Chem.* **2002**, *74*, 5742–5747. [CrossRef]
33. Gal-Or, L.; Silberman, I.; Chaim, R. Electrolytic ZrO_2 coatings: I. electrochemical aspects. *J. Electrochem. Soc.* **1991**, *138*, 1939–1941. [CrossRef]
34. Min, X.; Wu, X.; Shao, P.; Ren, Z.; Ding, L.; Luo, X. Ultra-high capacity of lanthanum-doped UiO-66 for phosphate capture: Unusual doping of lanthanum by the reduction of coordination number. *Chem. Eng. J.* **2019**, *358*, 321–330. [CrossRef]
35. Wang, J.; Peng, Y.; Xiao, W. Photocatalytic nonoxidative coupling of methane to ethylene over carbon-doped ZnO/Au catalysts. *Sci. China Chem.* **2023**, *66*, 3252–3261. [CrossRef]
36. Du, Y.; Jin, J.; Liang, H.; Jiang, W. Structural and physicochemical properties and biocompatibility of linear and looped polymer-capped gold nanoparticles. *Langmuir* **2019**, *35*, 8316–8324. [CrossRef]
37. Yasmin, M.; Gupta, M. Thermoacoustical analysis of solutions of poly(ethylene glycol) 200 through H-bond complex formation. *Thermochim. Acta* **2011**, *518*, 89–100. [CrossRef]
38. Ge, Y.; Li, M.; Zhong, Y.; Xu, L.; Lu, X.; Hu, J.; Peng, Q.; Bai, L.; Wen, Y. Halloysite nanotube/black phosphorene nanohybrid modified screen-printed carbon electrode as an ultra-portable electrochemical sensing platform for smartphone-capable detection of maleic hydrazide with machine learning assistance. *Food Chem.* **2023**, *406*, 134967. [CrossRef]
39. Khan, M.S.; Ameer, H.; Ali, A.; Li, Y.; Yang, L.; Ren, X.; Wei, Q. Electrochemiluminescence behaviour of silver/$ZnIn_2S_4$/reduced graphene oxide composites quenched by Au@SiO_2 nanoparticles for ultrasensitive insulin detection. *Biosens. Bioelectronics* **2020**, *162*, 112235. [CrossRef]
40. Shafi, M.A.; Bouich, A.; Khan, L.; Ullah, H.; Guaita, J.M.; Ullah, S.; Mari, B. Optimization of electrodeposition time on the properties of Cu_2ZnSnS_4 thin films for thin film solar cell applications. *Opt. Quantum Electron.* **2022**, *54*, 533. [CrossRef]
41. Dai, X.; Lu, L.; Zhang, X.; Song, Z.-L.; Song, W.; Chao, Q.; Li, Q.; Wang, W.; Chen, J.; Fan, G.-C.; et al. MnO_2 shell-isolated SERS nanoprobe for the quantitative detection of ALP activity in trace serum: Relying on the enzyme-triggered etching of MnO_2 shell to regulate the signal. *Sens. Actuators B Chem.* **2021**, *334*, 129605. [CrossRef]
42. Huang, J.; Zhao, H.; Chen, X.; Lin, T.; Hou, L.; Zhao, S. Pt nanoparticles functionalized hydrogen-bonded organic frameworks: A three-in-one nanozyme for colorimetric detection of alkaline phosphatase. *Spectrochim. Acta Part A Mol. Biomol. Spectrosc.* **2025**, *333*, 125894. [CrossRef] [PubMed]
43. Dong, Q.; Song, W.; Zhang, S.; Lin, X.; Shi, P. Cysteine-assisted synthesis of copper nanoclusters for construction of FRET-based ratiometric sensor for visual detection of alkaline phosphatase. *Talanta* **2025**, *291*, 127910. [CrossRef]
44. Li, Y.; Cai, Y.; Wang, Y.; Xue, R.; Ren, Z.; Liu, Y.; Chen, W.; Liu, Z.; Bao, X.; Huang, Z. A reusable copper-cysteamine fluorescence probe for cost-effective detection of alkaline phosphatase activity based on a redox-modulated inner filter effect. *Microchem. J.* **2025**, *209*, 112694. [CrossRef]
45. Wu, X.J.; Yang, C.P.; Jiang, Z.W.; Xiao, S.Y.; Wang, X.Y.; Hu, C.Y.; Zhen, S.J.; Wang, D.M.; Huang, C.Z.; Li, Y.F. A catalyst-free co-reaction system of long-lasting and intensive chemiluminescence applied to the detection of alkaline phosphatase. *Microchim. Acta* **2022**, *189*, 181. [CrossRef]
46. Li, S.; Li, J.; Geng, B.; Yang, X.; Song, Z.; Li, Z.; Ding, B.; Zhang, J.; Lin, W.; Yan, M. TPE based electrochemiluminescence for ALP selective rapid one-step detection applied in vitro. *Microchem. J.* **2021**, *164*, 106041. [CrossRef]
47. Qi, W.; Fu, Y.; Zhao, M.; He, H.; Tian, X.; Hu, L.; Zhang, Y. Electrochemiluminescence resonance energy transfer immunoassay for alkaline phosphatase using p-nitrophenyl phosphate as substrate. *Anal. Chim. Acta* **2020**, *1097*, 71–77. [CrossRef] [PubMed]

48. Zhou, X.; Jiang, Y.; Zhao, X.; Zhu, Y. A new two-photon ratiometric fluorescent probe for detecting alkaline phosphatase in living cells. *Molecules* **2016**, *21*, 1619. [CrossRef]
49. Green, O.; Eilon, T.; Hananya, N.; Gutkin, S.; Bauer, C.R.; Shabat, D. Opening a gateway for chemiluminescence cell imaging: Distinctive methodology for design of bright chemiluminescent dioxetane probes. *ACS Cent. Sci.* **2017**, *3*, 349–358. [CrossRef]

Disclaimer/Publisher's Note: The statements, opinions and data contained in all publications are solely those of the individual author(s) and contributor(s) and not of MDPI and/or the editor(s). MDPI and/or the editor(s) disclaim responsibility for any injury to people or property resulting from any ideas, methods, instructions or products referred to in the content.